Journal of Materials Chemistry A

ROYAL SOCIETY OF CHEMISTRY

PAPER

View Article Online
View Journal | View Issue

Cite this: J. Mater. Chem. A, 2024, 12, 30892

Ultra-low lattice thermal conductivity driven high thermoelectric figure of merit in Sb/W co-doped GeTe†

Khasim Saheb Bayikadi, [a] Safdar Imam,[a] Wei-Shen Tee, [b] Sugumaran Kavirajan, [a] Chiao-Yu Chang, [b] Amr Sabbah, [bc] Fang-Yu Fu,[d] Ting-Ran Liu,[d] Ching-Yu Chiang,[e] Dinesh Shukla, [f] Chien-Ting Wu, [g] Li-Chyong Chen, [dh] Mei-Yin Chou,*[b] Kuei-Hsien Chen *[bd] and Raman Sankar *[a]

High thermoelectric performance is a material challenge associated mainly with the manipulation of lattice dynamics to obtain extrinsic phonon transport routes, which can make the lattice thermal conductivity (κ_{lat}) intrinsically low by introducing multiple scattering mechanisms. The present study shows that the lattice-strain-induced phonon scattering resulting from microstructural distortions in GeTe-based compounds can enable ultralow lattice thermal conductivity. The unusual lattice shrinkage, W interstitials, W nanoprecipitates, and heavy elemental mass, in $Ge_{0.85}Sb_{0.1}W_{0.05}Te$ culminate in an ultralow lattice thermal conductivity of ~0.2 W m^{-1} K^{-1} at 825 K. Microstructural distortions in this Sb/W co-doped GeTe are found to be primarily associated with shorter W–Te bonding owing to the anomalous effect of the higher electronegativity of the W atoms. Furthermore, the increased electrical conductivity (σ) resulting from the enhanced vacancy formation caused by W doping and W interstitials synergistically contributes to optimization of the thermoelectric performance (ZT) to ~2.93 at 825 K. The thermoelectric efficiency (η) as high as ~17% has been obtained for a single leg in this composition at an operating temperature of 825 K, with an estimated device ZT value of ~1.38.

Received 31st July 2024
Accepted 19th September 2024

DOI: 10.1039/d4ta05332j

rsc.li/materials-a

Introduction

The growing global energy demand has increased the necessity for alternative energy technologies. Among the three alternative energy technologies (conversion, conservation, and storage), thermoelectric technology falls between the conversion and conservation categories. Energy conversion, such as from fuel to kinetic energy, dissipates a significant amount (two-thirds) of energy in the form of heat, which could be saved by using thermoelectric devices.[1] Thermoelectric materials that are environmentally friendly can transform waste heat into energy, and such a solid material design should have optimum carrier transport and minimal thermal transit.[2] The dimensionless figure of merit ($ZT = S^2\sigma/\kappa T$), which is largely responsible for improving thermoelectric performance, is governed by three material properties, namely, thermopower (S), electronic conductivity (σ), and thermal conductivity ($\kappa = \kappa_{ele} + \kappa_{lat}$) contributed by the carrier (κ_{ele}) and lattice (κ_{lat}).[3] With effective scattering mechanisms, the ultimate ultralow lattice thermal conductivity (κ_{lat}) might be formulated, which can scatter broadly across all phonon spectrum frequencies (low, medium, and high).[4,5] Materials with ground breaking performance need to be designed to provide whole phonon group scattering to achieve an ultralow κ_{lat} value, such as anisotropic behaviour in layered crystals,[3] hierarchical nano/meso-scale structural design,[4] creation of complex crystal structures,[6] liquid crystalline behaviour,[7,8] bond anharmonicity due to the presence of lone pairs,[9] and co-doping of substituents with ionic behaviour.[10]

Owing to its unique band structure, microstructures, grain boundaries, stacking faults, and point defects, GeTe has attracted much interest among mid-temperature thermoelectric compounds[11] and has potential advantages over other well-

[a]Institute of Physics, Academia Sinica, Nankang, Taipei, Taiwan 11529. E-mail: sankarraman@gate.sinica.edu.tw
[b]Institute of Atomic and Molecular Sciences, Academia Sinica, Taipei 10617, Taiwan. E-mail: chenkh@pub.iams.sinica.edu.tw
[c]Tabbin Institute for Metallurgical Studies, Tabbin, Helwan 109, Cairo 11421, Egypt
[d]Center for Condensed Matter Sciences, National Taiwan University, Taipei 10617, Taiwan
[e]National Synchrotron Radiation Research Center, Hsinchu City 30077, Taiwan
[f]UGC-DAE Consortium for Scientific Research, Indore 452001, India
[g]Taiwan Semiconductor Research Institute, Hsinchu Science Park, Hsinchu 300, Taiwan
[h]Center of Atomic Initiative for New Materials, National Taiwan University, Taipei 10617, Taiwan

† Electronic supplementary information (ESI) available. See DOI: https://doi.org/10.1039/d4ta05332j

known PbTe and SnSe thermoelectric compounds.[3,12] Owing to its inherent vacancies, GeTe has a low impact on the immaculate performance, yet it has proven to be the best alloy compound among PbTe,[13] SnTe,[14] $AgSbTe_2$,[15] and Cu_2Te–PbSe.[16] GeTe-based compounds have been extensively explored in the past decade owing to their vacancy control for optimized carrier concentration (n) with various dopants, among which the best aliovalent cation dopants (such as Bi or Sb)[17–20] continually reduce the carrier contribution to thermal conductivity (κ_{ele}). However, an evident contribution to the lattice thermal conductivity (κ_{lat}) of ~2.5–1.5 W m^{-1} K^{-1} at 300 K was confirmed using individually doped compounds. There is a large scope for reducing the lattice thermal conductivity (~0.5–0.3 W m^{-1} K^{-1}), which has been explored using multiple co-dopants including (Se–S),[5] (Bi–In),[18] (Bi–Pb),[19] (Sb–Mn),[21] (Sb–In),[22] (Sb–Pb),[23] (Sb–Cu),[24] (Sb–Ti),[25] (Sb–Cr),[26] (Sb–Bi),[27] (Bi–Mg),[28] and (Sn–S–Se).[29] Optimized carrier transport and thermal transport in doped-GeTe compounds have resulted in the highest thermoelectric performance (ZT) of ~2.5–2.6 in the mid-temperature range (700 K), proving that GeTe compounds are some of the best thermoelectric materials.[30,31]

The entropy effect of a material is governed by its lattice dynamics, which reduces the lattice contribution to minimal thermal conductivity (κ_{lat}), improving the thermoelectric performance.[29,30] GeTe with multiple dopants significantly reduces the κ_{lat} value by creating more disorder and a strained lattice that can enhance phonon scattering.[5,21,27,29] Owing to the dominance of entropy-driven atomic disorders, a ternary system compound will always have a lower κ_{lat} value compared to a binary system compound.[23,27,30] A strategic approach to vacancy control in GeTe[32] and the strain-induced morphological boundary generated by Sb-doped GeTe[20] has encouraged us to investigate co-substitution with heavy element tungsten (W). Comprehensive theoretical and experimental investigations were conducted to determine the impact of co-dopant W on the thermoelectric performance, focusing on the following questions: (a) Will W occupy the GeTe lattice? (b) What positions might W occupy in the GeTe lattice? (c) What is the maximum amount of W that can enter the GeTe lattice? (d) What microstructural changes can W cause? (e) How do substituted and interstitial W affect the transport properties of GeTe? (f) Does the nanoprecipitate contain phase-separated W? What are the primary effects of W in its various forms on κ_{lat}?

We investigated W-doped $Ge_{0.9}Sb_{0.1}Te$ exhibiting an ultralow κ_{lat} value which led to higher thermoelectric performance and efficiency. To improve understanding, the ultralow κ_{lat} value and higher efficiency (η) of $Ge_{0.85}Sb_{0.1}W_{0.05}Te$ were explored, with the W co-dopant found to create an additional local band and large scattering centres, such as point defects, microstructural changes, strained herringbone domain boundaries, nanoprecipitates, and a disordered lattice and boundaries. Although it is well established that inhomogeneous internal-strain fields create phonon scattering centres, this research shows that internal-strain may also, on average, soften a material's lattice, hence altering sound velocity and phonon dispersion. Microstructural defects and internal strain, in addition to phonon scattering, allow for more control over lattice thermal conductivity. Overall, an optimized power factor of ~36–38 μW m^{-1} K^{-2} and enhanced scattering have resulted in ultralow κ_{lat} values of ~0.42 (325 K)–0.2 (825 K) W m^{-1} K^{-1}, which correspond to the highest ZT values of ~2.85–2.93 at 825 K. Thermoelectric efficiencies as high as ~17% have been estimated for the p-type single leg device performance, with an average ZT value of ~1.85 in the temperature range of 400–800 K.

Results

High-frequency phonons can be significantly dispersed by point defects in solid solutions owing to mass and strain changes between the host and guest atoms. Therefore, point defects with substantial mass and strain contrasts are advantageous for reducing the κ_{lat} value. However, the point defect density of solid solutions is limited by the solubility of the solutes.[21,27,33] The large concentration of point defects in semiconductors with an intrinsically highly disordered crystal structure suggests that these might be promising thermoelectric materials.[21] As a result, phonon scattering may be further amplified owing to the substantial mass and size difference between Sb/Ge and W/Ge atoms. To further investigate the thermoelectric properties of $Ge_{0.85}Sb_{0.1}W_{0.05}Te$, we investigated its crystallographic features to determine whether a high ZT value could be obtained.

The κ_{lat} value of $Ge_{0.85}Sb_{0.1}W_{0.05}Te$ diminishes to ~0.2 W m^{-1} K^{-1} at 825 K, which is the lowest among known GeTe-based compounds, as shown in Fig. 1.[18,34] The lattice contribution to the thermal conductivity (κ_{lat}) of GeTe, $Ge_{0.9}Sb_{0.1}Te$, and $Ge_{0.85}Sb_{0.1}W_{0.05}Te$ samples was calculated by subtracting the κ_{ele} value from the κ_{total} value, with the κ_{lat} values shown in Fig. 1(a). The Cahill model, Clarke model, diffusion model, and Born–von Karman periodic boundary model have been used to derive the theoretical minimum κ_{lat} value of $Ge_{0.85}Sb_{0.1}W_{0.05}Te$, with results of ~0.47, 0.34, 0.29, and 0.19 W m^{-1} K^{-1}, respectively.[4,34] These findings suggest that the experimental minimum κ_{lat} value for the present Sb/W co-doped materials is below the so-called glass limit, approaching the diffusion limit reported by Snyder.[35] The observed κ_{lat} value of $Ge_{0.85}W_{0.05}Sb_{0.1}Te$ below 300 K was fitted using the Debye–Callaway model to better understand the effect of multiple phonon-scattering processes on the ultralow κ_{lat} value of Sb/W co-doped GeTe.[4] The contribution of several scattering processes to the decreased κ_{lat} value of $Ge_{0.85}W_{0.05}Sb_{0.1}Te$ is shown in Fig. 1(b). The results indicated that Sb/W co-doping creates large strain fields and mass fluctuations, despite suppressing the κ_{lat} value.[34]

The total phonon scattering relaxation time, τ, can be expressed as follows:

$$\tau^{-1} = \frac{V_s}{L} + A\omega^4 + B\omega^2 T e^{\frac{-\theta_D}{3T}} + C\omega^2 + \frac{D\omega^2}{(\omega^2 - \omega_0^2)^2} \quad (1)$$

where A, B, and C are constant parameters, V_s is the average acoustic velocity, θ_D is the Debye temperature, ω is the angular frequency, and ω_0 is the cut-off frequency. The terms in eqn (1) indicate grain boundary scattering (B), point defect scattering (PD), Umklapp process (U), stacking fault scattering (SF), charge and bond resonant scattering (RES), nanoprecipitates (NPs),

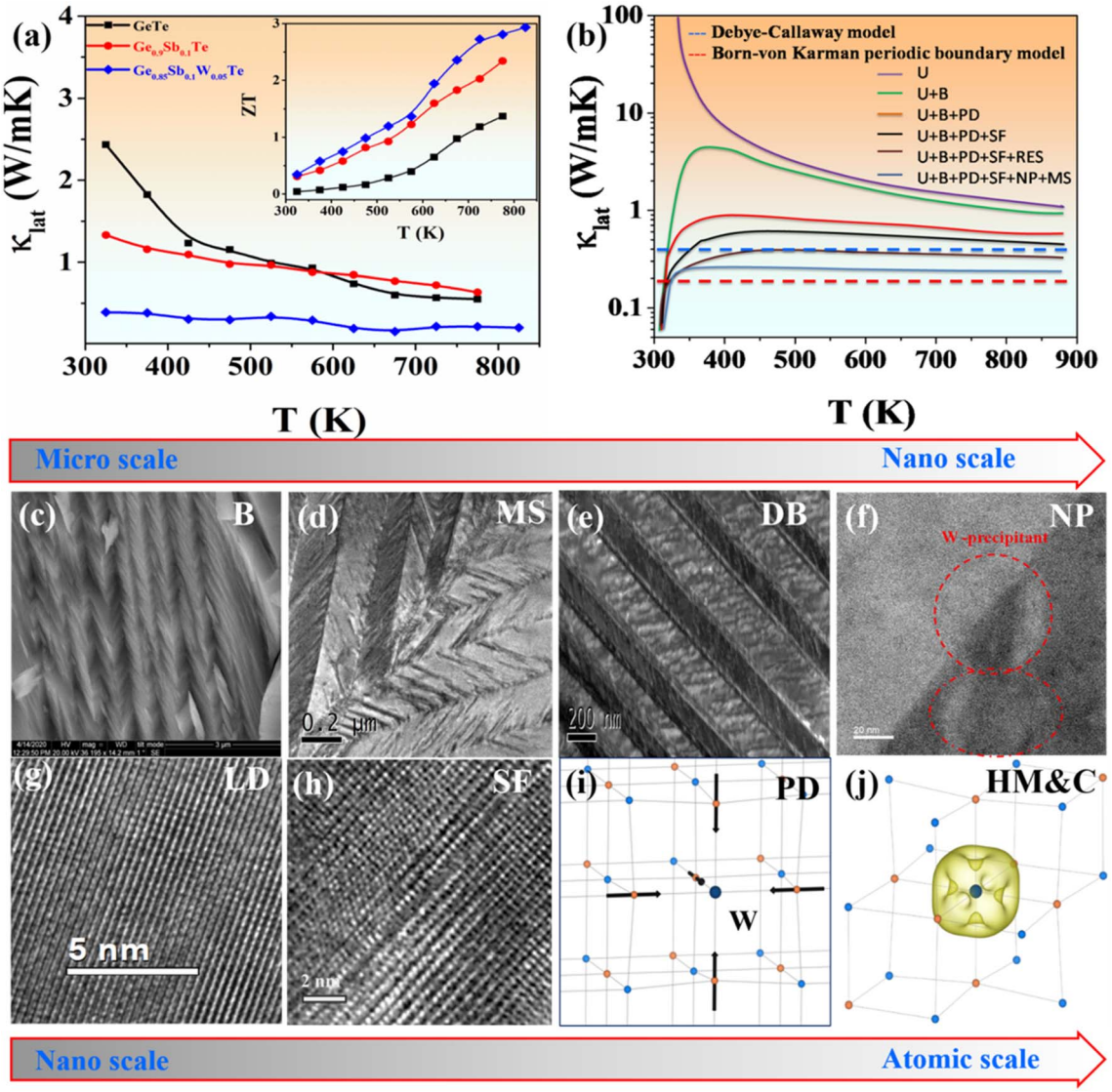

Fig. 1 (a) State-of-the-art reduction of lattice thermal conductivity (κ_{lat}) (inset, state-of-the-art systematic ZT enhancement); (b) the phonon–phonon Umklapp process (U), grain boundary scattering (B), point-defect scattering (PD), stacking fault scattering (SF), resonant phonon scattering (RES), nanoprecipitates (NPs), and microstructure scattering (MS) all contribute to the κ_{lat} value of $Ge_{0.85}Sb_{0.1}W_{0.05}Te$. (c–f) Micro-to-nano-level phonon scattering mechanism of micro grain boundaries (B), herringbone microstructure (MS), domain boundaries (DB), and nanoprecipitates (NPs); and (g–j) nano-to-atomic-level phonon scattering mechanism of lattice disorder, stacking faults, point defects, and heavy mass with lattice shrinkage and charge effects.

and microstructure scattering (MS). The amount of stacking flaws affects the phonon scattering parameter, C.[30]

$$\kappa_{lat} = \frac{k_B}{2\pi^2\vartheta}\left(\frac{k_B T}{\hbar}\right)\int_0^{\frac{\theta_D}{T}} \tau_C \frac{x^4 e^x}{(e^x-1)^2}\,dx \quad (2)$$

Eqn (2) corresponds to the Debye–Callaway model representing the minimum κ_{lat} value for the GeTe system in Fig. 1(a) (dashed line). The κ_{lat} values of all samples decreased with increasing temperature. Furthermore, the addition of Sb and W decreased the κ_{lat} value significantly. GeTe had a κ_{lat} value of ~2.43 W m^{-1} K^{-1} at 325 K, which was significantly reduced to ~0.4 W m^{-1} K^{-1} for $Ge_{0.85}Sb_{0.1}W_{0.05}Te$. Interestingly, GeTe co-doped with Sb and W showed a larger reduction in the κ_{lat} value compared with the controlled single-doped (Sb) GeTe samples (Fig. 1(a)). This significant reduction was attributed to synergistic phonon scattering caused by the observed 10–20 nm W nanoprecipitates and atomic-scale point defects resulting from mass fluctuations created by W replacing Ge in GeTe. W formed small nanoprecipitates in the GeTe matrix owing to the large size mismatch and solubility limit, while Sb preferred to form a solid solution in GeTe. Therefore, Sb and W have complementary roles in reducing the κ_{lat} value of GeTe. The overall micro-to-atomic scale phonon scattering mechanism is depicted in Fig. 1(c)–(j).

$$\tau_C^{-1} = \tau_U^{-1} + \tau_N^{-1} + \tau_B^{-1} + \tau_S^{-1} + \tau_D^{-1} + \tau_P^{-1} \quad (3)$$

Eqn (3) shows the overall relaxation time, where τ_U, τ_N, τ_B, τ_S, τ_D, and τ_P are the relaxation times corresponding to scattering from Umklapp processes, normal processes, boundaries, strains, dislocations, and precipitates.[4] Combining all the aforementioned scattering processes in the $Ge_{0.85}W_{0.05}Sb_{0.1}Te$ system significantly lowered the κ_{lat} value by ~0.2 W m^{-1} K^{-1}. The overall thermoelectric performance optimization studies are further discussed below.

Structural and elemental characterization

To confirm the bond length changes due to W substitution, we recorded the Fourier transformed EXAFS spectra for $Ge_{0.9}Sb_{0.1}Te$ and $Ge_{0.85}Sb_{0.1}W_{0.05}Te$ samples. As observed in Fig. 2(a), it should be noted that the similarities in photoelectron backscattering of Sb and Te make distinction between Ge–Sb and Ge–Te bonds in EXAFS data difficult;[36] thus, we focus only on Te EXAFS before and after introducing W. We can see the shortening of the bond length after W doping which can be attributed to the replacement of W with a Ge atom in the GST crystal system. The high-resolution TEM images of the $Ge_{0.85}Sb_{0.1}W_{0.05}Te$ sample in Fig. 2(b) clearly show W nanoprecipitation. The lattice changes due to W doping were confirmed by using Fast Fourier Transformation (FFT), shown in Fig. 2(b) and (c), revealing the GeTe (021) plane along with the existing W (200) plane. The lattice distance for the GeTe (021) plane dropped from ~3.42 Å (rhombohedral) and ~3.45 Å (cubic) to ~3.38 Å for the $Ge_{0.85}Sb_{0.1}W_{0.05}Te$ compound because of W bonding to Te. Also, the presence of an additional dot represented the W cubic (200) plane (mp-1134) lattice distance of ~2.48 Å, which originates from the nanoprecipitation.

We recorded X-ray absorption fine structure spectra for $Ge_{0.9}Sb_{0.1}Te$ (GST) and $Ge_{0.85}Sb_{0.1}W_{0.05}Te$ (WGST) to learn more about their crystal structures and the atomic occupancy of doping elements. As can be seen in Fig. 2(d), when compared with the X-ray absorption near-edge structure (XANES) of the Ge K-edge, the XANES of the Ge K-edge of $Ge_{0.9}Sb_{0.1}Te$ and $Ge_{0.85}Sb_{0.1}W_{0.05}Te$ shows hardly any difference between the two materials. Fig. 2(f) shows a comparison of the XANES spectra of the Sb K-edge in $Ge_{0.9}Sb_{0.1}Te$ and $Ge_{0.85}Sb_{0.1}W_{0.05}Te$. The behavior observed here was quite similar to that of the Ge K-edge. Since theoretical research shows that W-doping is predicted to reduce the bond length between Te and W atoms, XAS was used as a potent approach to analyse the local structure and

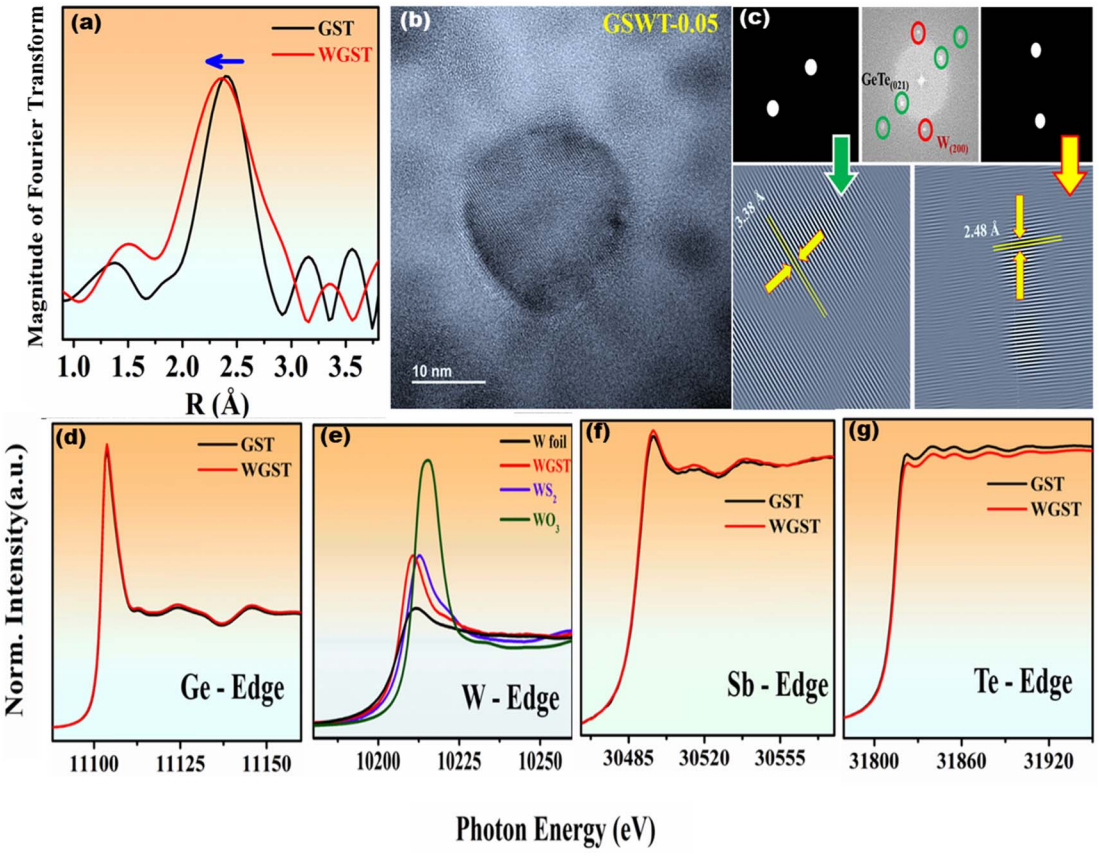

Fig. 2 (a) Fourier transformed EXAFS spectra of the *R* space of ground pellets GST (black) and WGST (red), (b) HR-TEM image of W nanoprecipitated $Ge_{0.85}Sb_{0.1}W_{0.05}Te$, and (c) Fast Fourier Transformation (FFT) with lattice analysis of the GeTe (021) plane and W (200) plane. (d) Experimental XANES spectra at the Ge K-edge for $Ge_{0.9}Sb_{0.1}Te$ (black line) and $Ge_{0.85}Sb_{0.1}W_{0.05}Te$ (red line). (e) Experimental XANES spectra at the W L-edge for different-oxidation state W foil (0) (black line), $Ge_{0.85}Sb_{0.1}W_{0.05}Te$ (+2) (red line), WS_2 (+4) (indigo line) and WO_3 (+6) (green line). (f) Experimental XANES spectra at the Sb K-edge for $Ge_{0.9}Sb_{0.1}Te$ (black line) and $Ge_{0.85}Sb_{0.1}W_{0.05}Te$ (red line). (g) Experimental XANES spectra at the Te K-edge for $Ge_{0.9}Sb_{0.1}Te$ (black line) and $Ge_{0.85}Sb_{0.1}W_{0.05}Te$ (red line).

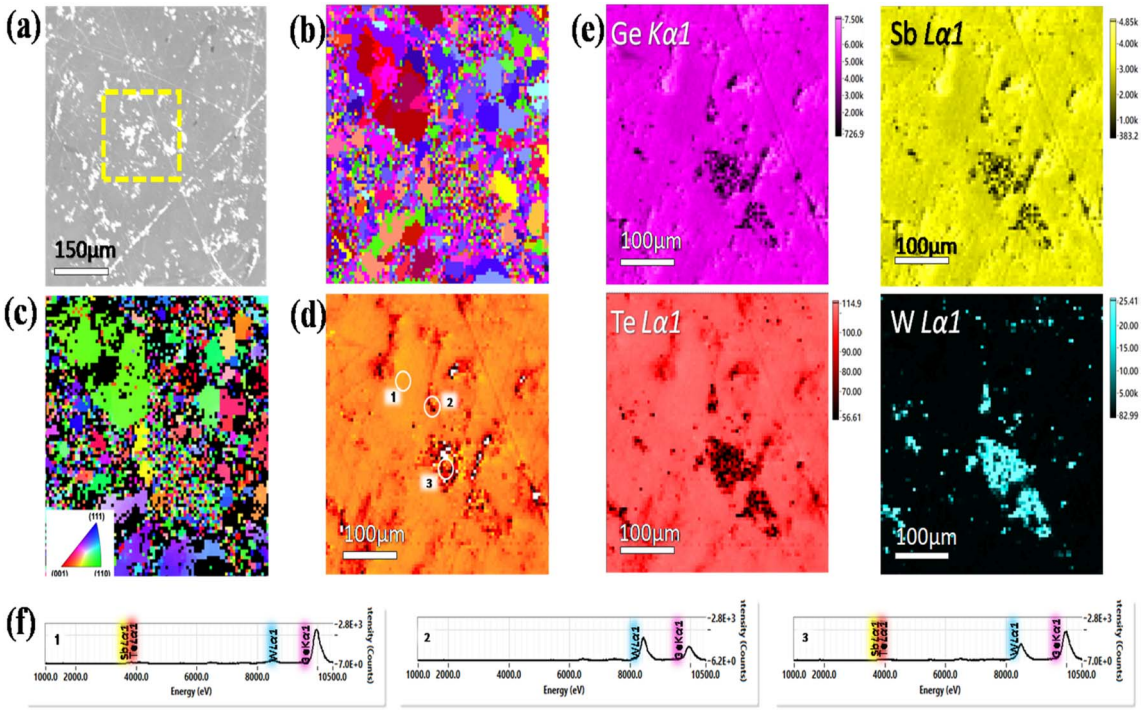

Fig. 3 (a) SEM of surface topography of the polished pellet, (b) orientation mapping of the yellow marked square in the SEM image, (c) inverse pole figure based on the cubic phase, (d) intensity map of the yellow marked square in the SEM image, (e) XRF maps of the constituent alloying elements (Ge, Sb, Te, and W), and (f) XRF spectrum of the highlighted region of the intensity map figure (d).

determine how W doping affects the Te K-edge. Te K-edge absorption spectra of $Ge_{0.9}Sb_{0.1}Te$ and $Ge_{0.85}Sb_{0.1}W_{0.05}Te$ are shown in Fig. 2(e). The electron densities of the Te K-edge XANES spectra clearly differ, demonstrating that W's high electronegativity significantly adjusts the Te bond length without producing a secondary phase telluride, confirming W doping at the Ge site. As shown in Fig. 2(g) tungsten L-edge X-ray absorption spectroscopy was used to probe a set of tungsten compounds covering the element's formal oxidation states from 0 to +VI.[37] To put it another way, the excitation probability of the black line in the metal (0) is less than that in the oxide because the metal's conductive band is already filled with electrons. However, after W doping ($Ge_{0.85}Sb_{0.1}W_{0.05}Te$), a change in intensity is still observed due to the increase in shared electron density, which is consistent with our theoretical findings. These spectra are helpful because their calculated correlations allow for an evaluation of the effective metal oxidation state (+2).[37]

The microstructural evolution was characterized using X-ray nano diffraction (XND) with a 90 × 90 nm^2 spot size to map the grain orientation, grain shape, and grain size. As described in Fig. 3(b), orientation mapping was conducted on the yellow marked square in the SEM image of the pellet surface (Fig. 3(a)). Fig. 3(c) shows the inverse pole figure of the sample direction relative to the cubic system.[38] The XND analysis revealed the orientations of the grains along the *z* direction in the sample pellet. The microstructure shows a bigger grain size as well as small fine grains which could be related to grains with enriched W ratios in accordance with the XRD results, particularly in areas where the W nanoprecipitates formed. For elemental distributions, we conducted an X-ray nanoprobe study to verify the existence of W at certain positions. The XRF maps (Fig. 3(e)) of the region indicated in the SEM image in Fig. 3(a) demonstrate near-uniform distribution of germanium, antimony, and tellurium within the scanning area. In contrast, tungsten shows a localized distribution along the grain boundaries. More specifically, we show the W spectrum in Fig. 3(f) of the region indicated in the intensity map image in Fig. 3(d). As shown in region 1, where there is no aggregation of W primarily in a big grain, the spectrum shows the presence of all 4 elements, with a low intensity of the W peak. However, in region 2, where the W precipitates are located, we can see a strong peak of W while Sb and Te are absent, indicating the presence of metallic W. On the other hand, region 3 shows the existence of all elements with a high ratio of W indicating the W precipitate along the small grains of $Ge_{0.85}Sb_{0.1}W_{0.05}Te$ as previously shown in the orientation map in Fig. 3(b).

Microstructural analysis

Microstructural changes in vacancy-controlled GeTe, Sb-substituted GeTe, and W-doped GeTe were investigated theoretically and experimentally. The results of experimental and theoretical analyses of the GeTe, $Ge_{0.9}Sb_{0.1}Te$, and $Ge_{0.85}Sb_{0.1}W_{0.05}Te$ samples are shown in Fig. 4. Fig. 4(a)–(c) show the GeTe microstructure controlled by vacancies,[32] Sb-substituted GeTe,[20] and W-co-doped $Ge_{0.85}Sb_{0.1}W_{0.05}Te$, respectively. Controlled Ge vacancies, as shown in Fig. 4(a), can reduce lattice shrinkage and enhance domain width. However, Ge vacancies can

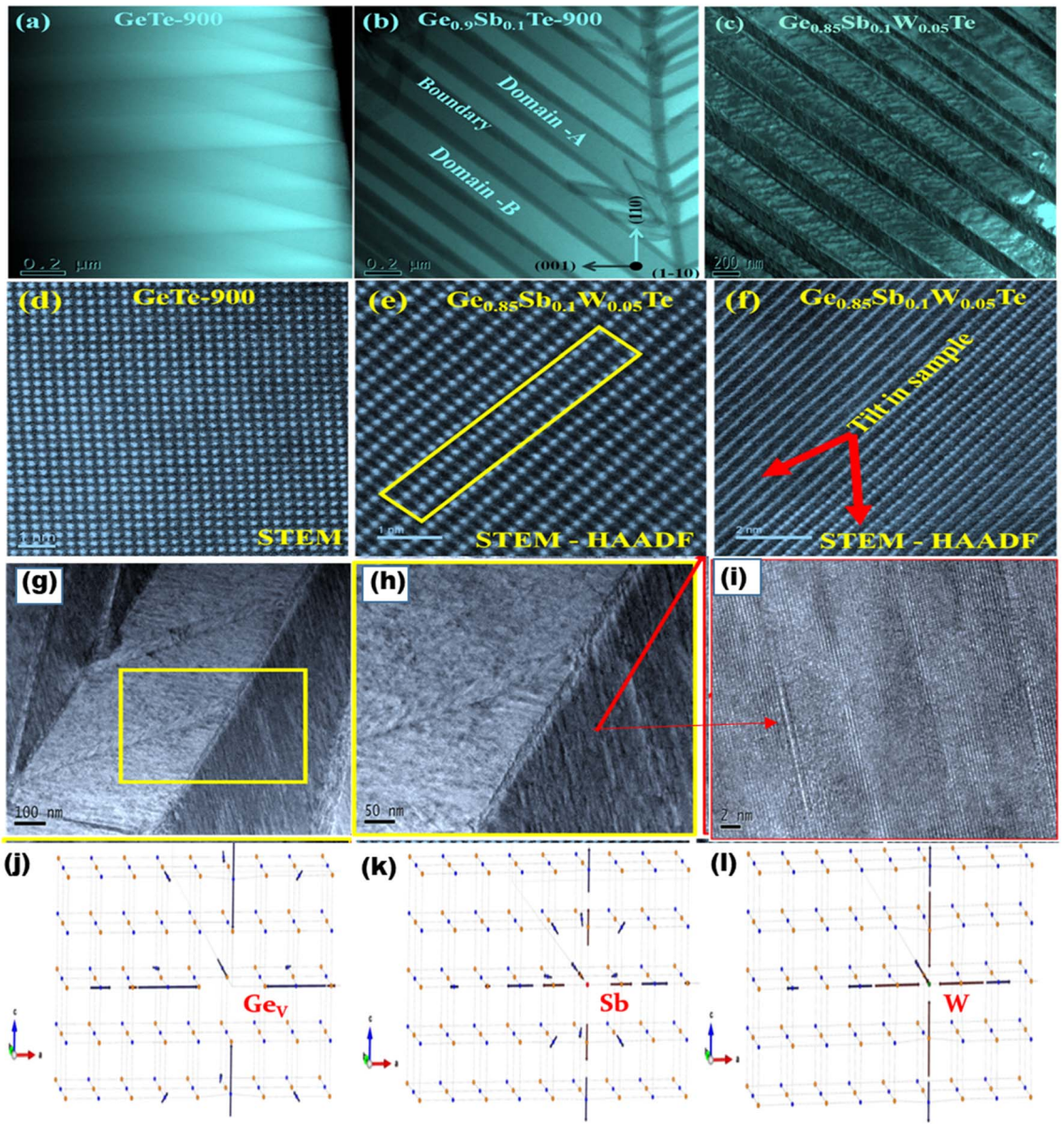

Fig. 4 Transmission electron microscopy images of (a) vacancy-controlled GeTe, (b) Sb-doped GeTe, and (c) W-codoped $Ge_{0.9}Sb_{0.1}Te$. Analysis of herringbone domains and strained boundaries of $Ge_{0.85}Sb_{0.1}W_{0.05}Te$: (d) herringbone domains and boundaries, (e) magnified view of domains and boundaries, and (f) atomic disorder in the domain lattice. High-angle annular dark-field (HAADF) scanning transmission electron microscopy (STEM) images of (g) GeTe, (h) $Ge_{0.9}Sb_{0.1}Te$, and (i) $Ge_{0.85}Sb_{0.1}W_{0.05}Te$. Atomic movement of the neighbouring atoms driven by (j) a vacancy, (k) Sb substitution, and (l) W substitution.

increase lattice shrinkage owing to the movement of neighbouring Te atoms towards the vacancy sites, as shown in Fig. 4(j), resulting in very narrow domains.[32] The high- and low-intensity peaks that appear correspond to the atomic sizes of different atoms (Ge, Sb, W, and Te). Fig. 4(d)–(f) show HAADF-STEM images of vacancy-controlled GeTe and $Ge_{0.85}Sb_{0.1}W_{0.05}$-Te compounds. Fig. 4(d) shows vacancy-controlled pristine GeTe with a uniform distribution of atoms, while Fig. 4(e) shows $Ge_{0.85}Sb_{0.1}W_{0.05}Te$ with highly occupied atomic sites. These contrasts and variations in atomic sizes showed that Ge atoms were replaced with heavy Sb/W atoms.[30] Fig. 4(f) shows a clear lattice view of the $Ge_{0.85}Sb_{0.1}W_{0.05}Te$ compound with a small tilt in the sample, demonstrating the existence of lattice strain in the crystal plane of the system. As shown in Fig. 4(k), Sb-doping at Ge sites induced strain by pushing out neighbouring Te atoms. Fig. 4(g) shows the existing herringbone structure with additional strained boundaries arising from different types of additional strain, including (Sb and W substitution) along with possible W interstitials. Fig. 4(h) shows a magnified view of the strained boundary and the situated strained domains. Fig. 4(i) shows a magnified view of the strained domain located with a different lattice *d*-spacing owing to the persisting strains, as discussed in Fig. 4. Fig. S10† shows a highly magnified view of lattice distortions caused by the strain mechanism. The insets of Fig. S10† show the highly occupied and more disordered lattice arrangements.

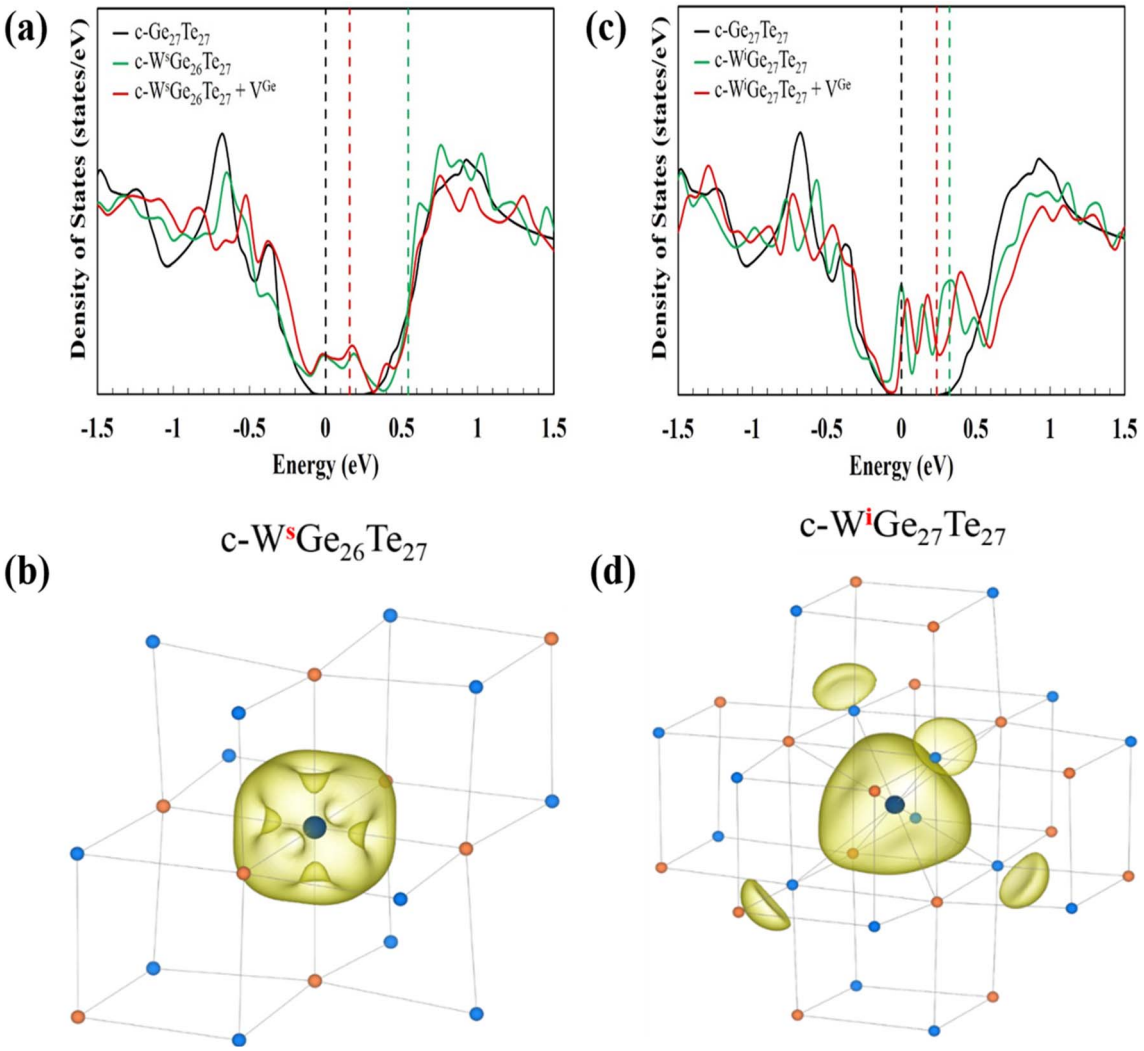

Fig. 5 Density of states (DOS) for cubic GeTe systems with the following configurations: (a) pristine GeTe (black), and doped GeTe with W substitution (W^s, blue) and (c) interstitial W (W^i, red). The energy zero (dashed line) is defined by the top of the valence bands of pristine GeTe. The band energy in the doped cases is aligned with the bottom of the Te 5s states in pristine GeTe. Solid vertical lines indicate the Fermi levels of each doped system. Charge density distributions on W atom: (b) for substituted W (d) for interstitial W.

This strain was released at the end of each domain, establishing consecutive tensile and compressive strained boundaries.[20,39] The present investigation of W-doping in $Ge_{0.9}Sb_{0.1}Te$ imposed an additional strain owing to the higher Pauling electronegativity (~2.36) of the W atom causing compression of its bond length with the Te atom, as shown in Fig. 4(l). This resulted in a shift in the microstructure from $Ge_{0.9}Sb_{0.1}Te$ to $Ge_{0.85}Sb_{0.1}W_{0.05}Te$, as shown in Fig. 5. The theoretical and experimental microstructural changes were virtually identical, including additional scattering of heavy element W point defects and strain contributing to the $Ge_{0.85}Sb_{0.1}W_{0.05}Te$ compound. As secondary confirmation, microstructural investigation showed that W entered the GeTe lattice.

Computational studies

We used first-principles simulations to investigate the function of W in GeTe. Based on ESI data,† we know that when W enters the GeTe structure, it occupies various sites. Table 1 summarizes the formation energies of W at various sites. In addition, W-doping may promote the formation of more Ge vacancies, which could lead to increased p-type doping (see Table 2).

Fig. 5 shows the theoretical investigation of spin–orbit coupling calculations, which revealed the band structure of pristine GeTe, W-doped GeTe, and W-interstitial GeTe compounds. Fig. S13† shows the partial density of states for pristine and W-interstitial GeTe compounds. Fig. S13(a)† shows

Table 1 Formation energies (eV) of W^s and W^i in GeTe, and in the presence of a Ge vacancy based on the configurations shown in Fig. 1. Calculations were performed using a 3 × 3 × 3 GeTe supercell

	W positions		W positions (with a Ge vacancy)			
	W^s	W^i	(i) W^s	(ii) W^s	(iii) W^i	(iv) W^i
Cubic	2.79	2.91	2.52	1.94	2.28	2.24
Rhombohedral	3.10	3.12	2.54	2.10	2.03	1.96

Table 2 Formation energy (eV) of a Ge vacancy in pristine GeTe and in the presence of a doped W atom. Calculations were performed using a 3 × 3 × 3 GeTe supercell

		Ge vacancy (with a W atom)	
	Ge vacancy	W^s	W^i
Cubic	0.27	−0.58	−0.40
Rhombohedral	0.56	−0.44	−0.60

the partial density of states for pristine GeTe, where the valence band (VB) is contributed by the Te p-orbitals and the conduction band (CB) is contributed by the Ge p-orbitals. The band structure of the W interstitials found in the GeTe compounds is shown in Fig. S13(b).† An increase in W interstitials will increase the number of local bands between the VB and CB, resulting in the generation of Ge vacancies, which ultimately enhances the metallic character of the system.

Fig. 5(a) shows the band structure of W-doped GeTe, where the Fermi level shifts from the VB to the CB, and some additional bands are generated from the W d-orbital. However, substitution with W atoms will decrease the formation of Ge vacancies, which eventually decreases the Fermi level further into the bandgap region. This shows that the W-doped GeTe system still maintained its p-type characteristic behaviour. In contrast, Fig. 5(b) shows charge density accumulation on the substituted W atom. Owing to their high electronegativity, the substituted W atoms will accumulate more charge density from the neighbouring Te atoms. Fig. 5(c) shows the W-substituted GeTe band structure, which shows the Fermi level shifting toward the CB with more interstitials. However, the theoretical calculations suggested that the possible Ge vacancies might further increase with W interstitials, eventually making the system more metallic in nature. Additional bands between the VB and CB were due to the contribution of W d-orbitals, but the calculated charge density distributions for W interstitials and neighbouring atoms were mostly localized, as shown in Fig. 5(d). These theoretical studies showed that the substituted and interstitial W atoms decreased the Ge vacancy formation energy and easily generated a higher carrier concentration (n) (holes) to contribute to charge transport. A more metallic character of the system was achieved due to the additional strain and defects introduced by the W atoms into the GeTe lattice, together with higher vacancy production. This increase in metallic nature and the effects of substitution, interstitials, and nanoprecipitates, on the system were further studied by investigating the temperature-dependent thermoelectric properties, which were in good agreement with the theoretical and microstructural effects.

Carrier transport studies

We investigated the temperature-dependent transport characteristics of electrical conductivity, Seebeck coefficient, and power factor using hot-pressed samples. Samples with a W-doping concentration of less than 2 atom% were prepared and their transport properties were examined to validate the W-doping concentration in the Ge sites. The temperature-dependent carrier transport features of low W concentration (x < 2 atom%) samples are shown in Fig. S14.† The temperature-dependent electrical conductivity (σ) of $Ge_{0.9-x}Sb_{0.1}W_xTe$ samples (x = 0.0075–0.015) is shown in Fig. S14(a).† When W concentration was increased from 0.0075 to 0.1, the lowest σ value (580 S cm^{-1}) was obtained at 325 K. Subsequent increases in the W concentration resulted in increased σ values. This trend in the σ value indicates that only a small quantity of W occupies the Ge sites, estimated to be approximately <1.5 atom%. For all samples, the σ value increased considerably after the phase transition (pseudo cubic to cubic phase, 525–625 K). The temperature-dependent Seebeck coefficient of $Ge_{0.9-x}Sb_{0.1}W_xTe$ samples (x = 0.0075–0.015) is shown in Fig. S14(b).† The comparative S values of all samples showed favourable alignment of the VB (L and Σ) with more valleys, which contributed to the effective mass (m^*), and heavy W doping reduced mobility (μ).[22] Fig. S14(c)† shows the temperature-dependent power factor of $Ge_{0.9-x}Sb_{0.1}W_xTe$ samples (x = 0.0075–0.015). Except for a W concentration of ∼1 atom%, all samples showed a power factor relatively comparable to that of pristine $Ge_{0.9}Sb_{0.1}Te$. The following results validated the doping limit concentration of W at the Ge sites, and the transport characteristics of samples with greater W concentrations were investigated further (2–6 atom%).

The temperature-dependent charge transport properties of $Ge_{0.9-x}Sb_{0.1}W_xTe$ samples (x = 0.02–0.06) are shown in Fig. 6(a)–(c). Fig. 6(a) shows the temperature dependent σ values of the samples. With increasing W concentration up to 4 atom%, the samples showed a systematic increase in σ values, while an abrupt increase was observed at a W concentration of 5 atom%. At 6 atom% W, the metallic nature of the system was enhanced. The metallic character of the samples supported the computational analyses. For the $Ge_{0.84}Sb_{0.1}W_{0.06}Te$ sample, a large increase in the σ value was observed. These results showed that the optimum limit of W in $Ge_{0.9}Sb_{0.1}Te$ was <6 atom%, with the significant contribution to σ also accounting for the increase in the κ_{ele} value in thermal transport. Fig. S15† shows the relationship between W concentration and carrier concentration (n) as well as mobility (μ). A systematic increase in the carrier concentration was clearly observed with increasing W concentration. At ∼6 atom% W, an enormous change was observed. More W incorporation enhanced the metallic nature of the $Ge_{0.9}Sb_{0.1}Te$ system. The experimental results of carrier concentration (n) and σ values are shown in Table 3.

Fig. 6(b) shows the temperature-dependent Seebeck coefficient (S) of the $Ge_{0.9-x}Sb_{0.1}W_xTe$ samples (x = 0.02–0.06). According to the Mott formula, an increase in the σ value always affects the S value because they are interconnected parameters, expressed as:

$$S \propto \frac{m^*}{n^{2/3}} \quad (4)$$

where m^* and n are the effective mass and carrier concentration, respectively. Except for W at ∼2 atom%, all samples

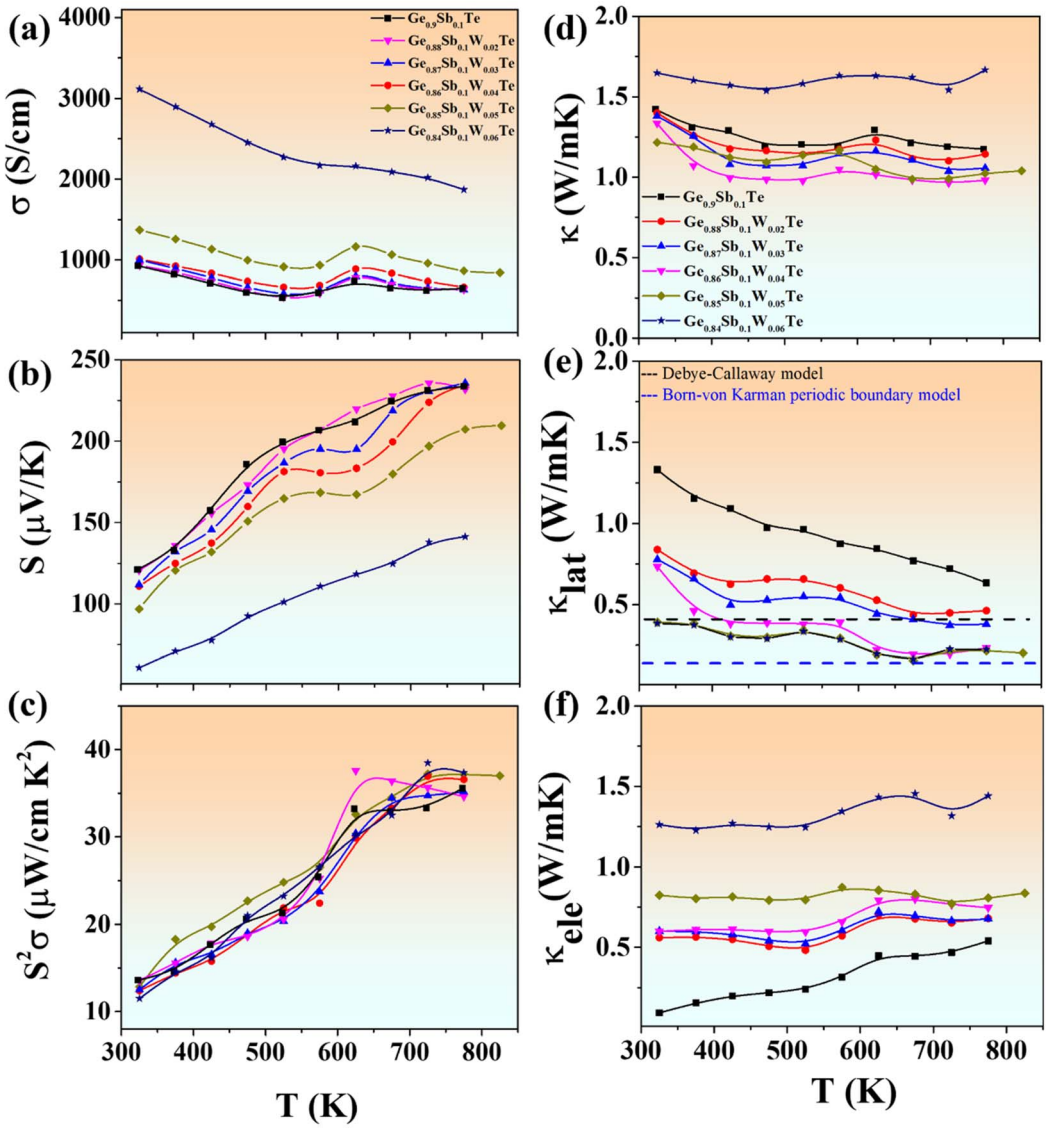

Fig. 6 (a–c) Temperature-dependent electronic transport properties of $Ge_{0.9-x}Sb_{0.1}W_xTe$ compounds: (a) electrical conductivity (σ), (b) Seebeck coefficient (S) and (c) power factor ($S^2\sigma$). (d–f) Thermal transport properties of $Ge_{0.9-x}Sb_{0.1}W_xTe$ compounds: (d) total thermal conductivity (κ_{tot}), (e) lattice thermal conductivity (κ_{lat}), and (f) electronic thermal conductivity (κ_{ele}).

showed a systematic decrease in S values. Meanwhile, W at 6 atom% showed a huge reduction in the S value. This reflected that the effect of W substitution and interstitials on Ge vacancy formation will increase above 2 atom% of W and more drastically above 4 atom% of W, further confirming that the doping limit of W is ~2 atom%. As observed in samples with higher W contents, the decreased temperature-dependent Seebeck coefficient is in good agreement with the increased carrier concentration from Fig. S11† and the computational investigations. The higher effective mass (m^*) and reduced mobility (μ) will help prevent the S values from collapsing as the carrier concentration increases at room temperatures. Fig. 6(c) shows the temperature-dependent overall carrier transport performance ($S^2\sigma$) of $Ge_{0.9-x}Sb_{0.1}W_xTe$ samples. The power factor is a binary product, with increased and decreased values of σ and S yielding overall comparable values for all samples. However, $Ge_{0.88}Sb_{0.1}W_{0.02}Te$ showed a stable power factor value of ~36–37 $\mu W\ cm^{-1}\ K^{-2}$ in the range of 625–775 K. Table 3 summarizes the experimentally determined values of n, σ, S, m^*, and μ at 325 K.

Thermal transport studies

Fig. 6(d)–(f) show the temperature-dependent thermal transport properties of the $Ge_{0.9-x}Sb_{0.1}W_xTe$ samples (x = 0.02–0.06). Fig. 6(d) shows the total thermal conductivity (κ_{tot}) of the samples. The overall thermal conductivity of the samples decreased with W doping of up to 4 atom%, while further increasing the W content resulted in an increase in thermal conductivity. For $Ge_{0.86}Sb_{0.1}W_{0.04}Te$, the lowest thermal conductivity of ~1 $W\ m^{-1}\ K^{-1}$ was observed, while the sample with a W content of ~0.06% showed the highest thermal conductivity of ~1.75 at 775 K. Fig. 6(e) reveals the lattice-contributed thermal conductivity (κ_{lat}) calculated from $\kappa_{lat} = \kappa_{tot}$

Table 3 Thermoelectric transport characteristics of W-doped $Ge_{0.9}Sb_{0.1}Te$

Compound	n ($\times 10^{20}$ cm^{-3})	μ (cm^{-2} V^{-1} s^{-1})	m^* (m_e)	σ (S cm^{-1})	S (μV K^{-1})
GeTe	7.33	70.54	1.28	8228	33
$Ge_{0.9}Sb_{0.1}Te$	0.84	68.74	1.15	927	121
$Ge_{0.89}Sb_{0.1}W_{0.01}Te$	0.85	41.19	1.08	560.93	121.8
$Ge_{0.88}Sb_{0.1}W_{0.02}Te$	1.07	54.38	1.25	932.27	120
$Ge_{0.87}Sb_{0.1}W_{0.03}Te$	1.65	37.80	1.55	999.23	111.9
$Ge_{0.86}Sb_{0.1}W_{0.04}Te$	2.4	26.26	1.98	1009.67	110.8
$Ge_{0.85}Sb_{0.1}W_{0.05}Te$	4.0	21.39	2.43	1370.94	96.82
$Ge_{0.84}Sb_{0.1}W_{0.06}Te$	8.5	22.87	2.52	3114.82	60.76

$-\kappa_{ele}$. In describing heat transport, particularly when the chemical composition is affected, it is now believed that structural flaws predominantly reduce thermal conductivity *via* phonon scattering, impacting both phonon dispersion and speed of sound.[40] Sound velocity is shown to decay linearly with increasing internal strain, as shown in Fig. S16† through experimental work on a GeTe compound system. This lattice softening, caused by the introduction of new phonon scattering mechanisms from nano and microstructural alterations and secondary heavy metal nanoprecipitates, is responsible for the overall decrease in lattice thermal conductivity.[40,41] A systematic decrease in thermal conductivity was observed with an increasing W content inside the $Ge_{0.9}Sb_{0.1}Te$ system. The lowest lattice thermal conductivities were observed for compositions with W contents of 0.05–0.06. The obtained lattice thermal conductivity values were between the limits of both theoretical models, namely, the Debye–Callaway model (0.4 W m^{-1} K^{-1}) and Born–von Karman periodic boundary model (0.2 W m^{-1} K^{-1}). [14,18,34,41] Fig. S17(d)† shows the measured thermal diffusivity (D). It is evident that co-doping with W along with Sb can significantly reduce thermal diffusivity (D). Furthermore, Fig. S17(d)† shows the measured specific heat (C_p) for $Ge_{0.85}Sb_{0.1}W_{0.05}Te$ compared with the C_p estimated using the Delong Petit law. As can be seen, the measured C_p varies within the error bar limit for all three batches of samples for heating and cooling cycles, and the C_p estimated using the Delong–Petit law approaches the average value of the measured results. Temperature independent ultra-low lattice thermal conductivity (κ_{lat}) was observed by Jiang *et al.*; the lattice softening as well as reductions in sound velocity will lead to ultra-low thermal conductivity.[14,40–44] The lowest lattice thermal conductivity of ~0.2 W m^{-1} K^{-1} was obtained for $Ge_{0.85}Sb_{0.1}W_{0.05}Te$ at 725–825 K.[4,5,7,29] With the presence of point defects (Ge/Sb/W), stacking faults, nanoprecipitates, herringbone domains, domain boundaries, strained lattice, mass fluctuations, and twin domains, all existing scattering mechanisms will reduce the overall lattice thermal conductivity to the lower limit.[4,10,18,27] Fig. 6(f) shows the electronic contribution to the thermal conductivity of W co-doped $Ge_{0.9}Sb_{0.1}Te$ samples. The electronic contribution to thermal conductivity is calculated from the Wiedemann–Franz law ($\kappa_{ele} = L_0\sigma T$; L_0, Lorentz number). The overall electronic contribution to the thermal conductivity increased with the increasing W concentration in the sample. The highest electronic contribution of ~1.4 W m^{-1} K^{-1} was achieved for the $Ge_{0.85}Sb_{0.1}W_{0.05}Te$ sample at 775 K. Fig. S20† shows the lattice thermal conductivity (κ_{lat}) of GeTe-based compounds with different combinations of doping. Co-doping W with GeSbTe clearly reduces the lattice thermal conductivity to a minimum.

State of the art: thermoelectric performance

The high and stable ZT value of more than 2 realized in $Ge_{0.9-x}Sb_{0.1}W_xTe$ largely originated from optimized carrier transport, along with the remarkable reduction in the κ_{lat} value caused by strategically induced lattice dynamic strains, boundaries, precipitates, and heavy point defects, resulting in more or less converged bands. Fig. 7(a) shows the overall thermoelectric performance of the W-doped $Ge_{0.9}Sb_{0.1}Te$ compounds, with the overall highest ZT value of ~2.93 at 825 K observed for $Ge_{0.85}Sb_{0.1}W_{0.05}Te$. Fig. 7(b) shows the state-of-the-art average ZT enhancement compared with the highest values reported for GeTe-based compounds. The present system synergistically enhanced the average ZT value to 1.8 in the temperature range of 400–800 K. This is the highest ever reported average ZT value for any element-doped GeTe-based compounds. Fig. 7(c) shows the thermoelectric efficiency of the system in different temperature ranges. However, the efficiency of thermoelectric energy conversion (η) is largely determined by the material's average figure of merit ($\overline{ZT}$):

$$\eta = \frac{T_h - T_c}{T_h}\left(\frac{\sqrt{1+\overline{ZT}}-1}{\sqrt{1+\overline{ZT}}+\frac{T_c}{T_h}}\right) \quad (5)$$

where T_h and T_c are the hot- and cold-end temperatures of thermoelectric materials, respectively, $\bar{T}$ is the average temperature of T_h and T_c, and ($\overline{ZT}$) is the average figure-of-merit for each thermoelement (p- and n-type). Conventionally, the peak ZT value is used to evaluate the compatibility of thermoelectric materials with device applications. However, the peak ZT value does not guarantee high efficiency. To obtain a high-efficiency thermoelectric generator (TEG), the average ($\overline{ZT}$) value over the working temperature range is a more important parameter. The present compound exhibited the highest thermoelectric efficiency for a single leg, reaching 17% at 825 K.

$$ZT_{device} = \left(\frac{T_h - T_c\,(1-\eta)}{T_h(1-\eta) - T_c}\right)^2 - 1 \quad (6)$$

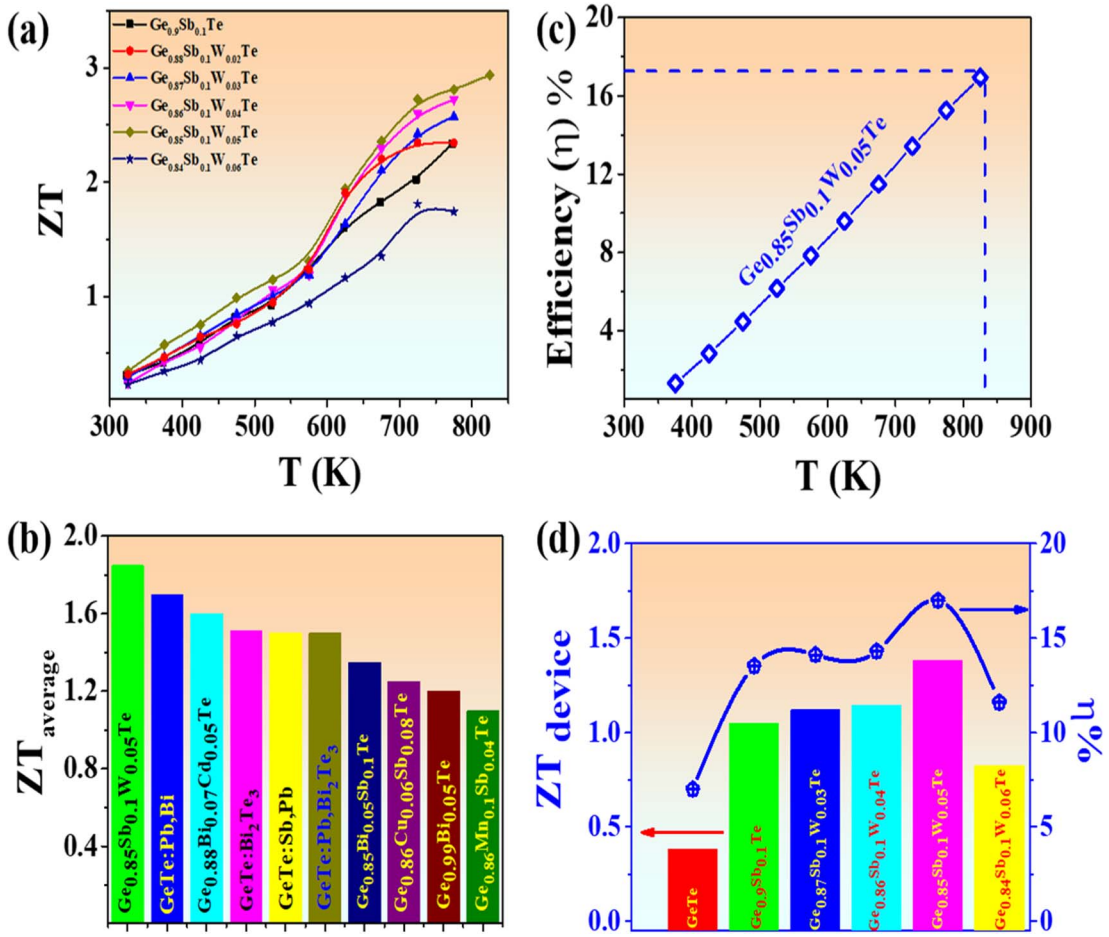

Fig. 7 (a) Temperature-dependent thermoelectric performance (*ZT*) of $Ge_{0.9-x}Sb_{0.1}W_xTe$ compounds, (b) average *ZT* values of state-of-the-art GeTe-based compounds, (c) thermoelectric efficiency of $Ge_{0.85}Sb_{0.1}W_{0.05}Te$ compounds in the overall temperature range (325–825 K), and (d) state-of-the-art efficiency enhancement and device *ZT* values for GeTe compounds.

Eqn (6) represents the device figure of merit.[45,46] Fig. 7(d) shows state-of-the-art materials, ranging from pristine GeTe to Sb-doped and W-doped GeTe systems, and the systematic increase in thermoelectric efficiency and device *ZT* values up to 5 atom% of W. Further incorporation of W might drastically reduce the device *ZT* value and efficiency owing to its highly metallic nature. Overall, the highest device *ZT* value of 1.38 and an efficiency of 17% were achieved using the $Ge_{0.85}Sb_{0.1}W_{0.05}Te$ compound. Moreover, the thermoelectric characteristics of $Ge_{0.85}Sb_{0.1}W_{0.05}Te$ exhibit excellent repeatability, and the *ZT* value remains consistent despite its uncertainty (Fig. S17†).

Conclusion

Theoretical strain inducement modelling, and experimental verifications together confirm that heavy element substitution-induced strain synergistically optimizes both electrical and thermal transport properties for achieving higher *ZT*, as demonstrated by W doping in the $Ge_{0.9}Sb_{0.1}Te$ system. The current work investigated microstructural changes in $Ge_{0.9-x}W_xSb_{0.1}Te$ materials and their thermoelectric characteristics in detail. It is shown that the high electronegativity of W can induce an extraordinary strain due to a decreased bond length between W and Te atoms. The lattice dynamics are significantly altered by heavy element doping. Besides complexation, nanoprecipitation leads to highly crystalline strained domains and disordered boundaries. The doped GeTe compounds have lattice thermal conductivities of ~0.4–0.2 W m^{-1} K^{-1}, which correlate with their final *ZT* values. The entire phonon spectrum is screened out by heavy W point defects, strained domains with disordered boundaries, stacking faults, interstitials, nanoprecipitates, and surface defects, elevating the *ZT* values to ~2.93 at 825 K. In the range of 400–800 K, the average *ZT* value achieved is higher than the reported value (~1.8). With a device *ZT* value of ~1.38 at 825 K, the anticipated single-leg efficiency is ~17%, which is the highest among reported so far.

Methods

Experimental procedure

Polycrystalline bulk samples of W co-doped $Ge_{0.9}Sb_{0.1}Te$ were prepared by combining stoichiometric amounts of highly pure (99.999%) germanium (Ge), tellurium (Te), antimony (Sb), and tungsten (W) in quartz ampoules under a vacuum of 10^{-4} mbar. The samples were heated and melted at 973 K for 24 h and then

cooled and crushed into extremely fine powders. The powders were then doubly sealed in quartz ampoules (to avoid compositional changes) and annealed at 1173 K for 48 h before quenching with air. The resulting ingots were ground into fine powder and then formed into high-density pellets by hot-press sintering at 820 K for 15 min under a vacuum of 10^{-5} mbar (to minimize oxidation) using a 15-mm graphite die under a pressure of 50 MPa. The Archimedes method was used to determine the densities of the heavily compressed pellets (~98% of the theoretical density). To measure electrical and thermal transport characteristics, the pellets were chopped and polished into rectangular ($12 \times 3 \times 3$ mm^3) or square pieces ($6 \times 6 \times 2$ mm^3).

Structural and chemical characterization

The presence of the secondary phase in the powder and hot-pressed pellet forms was validated by powder X-ray diffraction (PXRD) using a Bruker D8 diffractometer equipped with Cu K_α radiation ($\lambda = 1.5406$ Å). X-ray photoelectron spectroscopy (XPS) was performed using a PerkinElmer Physical Electronics PHI 5400 spectrometer equipped with a mono X-ray gun (Al) and a spherical electron energy analyzer with microscale X-ray focusing range capabilities. The carbon 1s peak at 284.6 eV was used to calibrate the XPS peak positions. Field-emission scanning electron microscopy (FESEM) with energy dispersive spectroscopy (EDAX) was used to confirm the elemental compositions (JEOL JSM-6700F). High-resolution transmission electron microscopy (HRTEM) was performed on the materials using Tecnai G2 F30 STWIN and JEOL JEM-ARM300F2TEM instruments, both equipped with a field emission gun capable of operating at 300 kV. X-ray absorption spectroscopy (XAS) was measured at beamline TLS 01C1 of the National Synchrotron Radiation Research Center facility in Taiwan. The Ge K-edge, Sb K-edge, and Te K-edge were recorded using transmission mode. The W L3-edge spectra were collected in fluorescence mode. The XANES spectra and EXAFS were plotted using the Athena program. GIWAXS was performed at beamline TLS 23A1. X-ray fluorescence spectroscopy (XRF) and orientation mapping were conducted using synchrotron nano diffraction (beamline 21A, Taiwan Photon Source (TPS)).

Computational calculations

First-principles calculations were performed to investigate the doped GeTe systems. Vienna *ab initio* simulation software (VASP)[47,48] with projector augmented wave (PAW) pseudo potentials was used. [49,50] The generalized gradient approximation (GGA)[51] was used for the exchange-correlation functional. Different configurations in a $3 \times 3 \times 3$ supercell of GeTe (originally 54 atoms) containing a W atom were considered. We used a plane-wave energy cutoff of 300 eV to ensure convergence. A Γ-centred $4 \times 4 \times 4$ k-mesh for the supercell was adopted for self-consistent calculations, while a Γ-centred $8 \times 8 \times 8$ k-mesh was used for density-of-states calculations. Spin–orbit coupling (SOC) was not included in atomic relaxation calculations but was included in all subsequent self-consistent calculations. The structure was fully relaxed using an energy criterion of 10^{-4} eV per cell between two steps. The VESTA program[52] was used for structure visualization. We used the tetrahedron method with Blöchl corrections[53] for Brillouin zone integration.

Measurement of thermoelectric properties

The thermal diffusivity (D) and specific heat (C_p) of the sintered pellets were measured using the laser flash technique (LFA-457, NETZSCH) with reference to Pyroceram standard calibration and calculated using $\kappa = DC_p\rho$, whereas D, C_p, ρ and represents the thermal diffusivity, specific heat, and density, respectively. The electrical thermal conductivity (κ_{ele}) was obtained using the Wiedemann–Franz law, $\kappa_{ele} = L\sigma T$, and the lattice thermal conductivity (κ_{lat}) was computed using the equation $\kappa_{lat} = \kappa_{tot} - \kappa_{ele}$, where L is the Lorenz number calculated using the empirical formula $1.5 + \exp\left(-\frac{|S|}{116}\right)$, where S is the Seebeck coefficient. The thermal conductivity was believed to have a ±5% margin of error. The carrier transport characteristics were tested using a parallelepiped-shaped ($3 \times 2 \times 15$ mm^3) pellet that was cut and polished in a helium gas environment, and S was measured concurrently on a ZEM-3 instrument (ULVAC), with the measurement accuracy estimated to be within ±5% for each parameter. In a magnetic field of up to 5 T, the Hall coefficient (R_h) was measured by the PPMS AC transport 5-point probe method. The carrier concentration (n) and mobility (μ) were calculated using the equations $n = 1/(eR_h)$ and $\mu = \sigma R_h$, where e is the electron charge.

Data availability

The data supporting this article have been included as part of the ESI.†

Conflicts of interest

The authors declare no conflicts of interest.

Acknowledgements

The all authors gratefully acknowledge the AS-SS-113-01 Project funding for research on thermoelectric materials for sustainable energy. R. S. acknowledges the financial support provided by the Ministry of Science and Technology in Taiwan under Project No. NSTC-113-2124-M-001-003, No. NSTC-113-2112-M001-045-MY3, and No. NSTC113-2124-M-A49-003 as well as support from Academia Sinica for the budget of AS-iMATE-11312. R. S. and L.-C. C. acknowledges financial support from the Center of Atomic Initiative for New Materials (AIMat), National Taiwan University, and from the Featured Areas Research Center Program within the framework of the Higher Education Sprout Project by the Ministry of Education in Taiwan under Project No. 113L900801. The authors thank the National Synchrotron Radiation Research Center (NSRRC) team for the beamline of X-ray nanodiffraction (TPS 21A), Taiwan Photon Source (TPS).

References

1 J. Mao, H. Zhu, Z. Ding, Z. Liu, G. A. Gamage, G. Chen and Z. Ren, *Science*, 2019, **365**, 495–498.

2 G. Tan, L.-D. Zhao and M. G. Kanatzidis, Rationally Designing High-Performance Bulk Thermoelectric Materials, *Chem. Rev.*, 2016, **116**, 12123–12149.

3 L. D. Zhao, S. H. Lo, Y. Zhang, H. Sun, G. Tan, C. Uher, C. Wolverton, V. P. Dravid and M. G. Kanatzidis, Ultralow thermal conductivity and high thermoelectric figure of merit in SnSe crystals, *Nature*, 2014, **508**, 373–377.

4 K. Biswas, J. He, I. D. Blum, C. I. Wu, T. P. Hogan, D. N. Seidman, V. P. Dravid and M. G. Kanatzidis, *Nature*, 2012, **489**, 414–418.

5 M. Samanta and K. Biswas, *J. Am. Chem. Soc.*, 2017, **139**, 9382–9391.

6 V. Dusastre, *Materials for Sustainable Energy: A Collection of Peer-Reviewed Research and Review Articles from Nature Publishing Group*, 2010, DOI: **10.1142/7848**.

7 B. Li, H. Wang, Y. Kawakita, Q. Zhang, M. Feygenson, H. L. Yu, D. Wu, K. Ohara, T. Kikuchi, K. Shibata, T. Yamada, X. K. Ning, Y. Chen, J. Q. He, D. Vaknin, R. Q. Wu, K. Nakajima and M. G. Kanatzidis, *Nat. Mater.*, 2018, **17**, 226–230.

8 H. Liu, X. Shi, F. Xu, L. Zhang, W. Zhang, L. Chen, Q. Li, C. Uher, T. Day and G. Snyder Jeffrey, *Nat. Mater.*, 2012, **11**, 422–425.

9 D. T. Morelli, V. Jovovic and J. P. Heremans, *Phys. Rev. Lett.*, 2008, **101**, 035901.

10 A. A. Olvera, N. A. Moroz, P. Sahoo, P. Ren, T. P. Bailey, A. A. Page, C. Uher and P. F. P. Poudeu, *Energy Environ. Sci.*, 2017, **10**, 1668–1676.

11 X. Zhang, Z. Bu, S. Lin, Z. Chen, W. Li and Y. Pei, *Joule*, 2020, **4**, 986–1003.

12 Y. Wu, Z. Chen, P. Nan, F. Xiong, S. Lin, X. Zhang, Y. Chen, L. Chen, B. Ge and Y. Pei, *Joule*, 2019, **3**, 1276–1288.

13 Z. Z. Luo, X. Zhang, X. Hua, G. Tan, T. P. Bailey, J. Xu, C. Uher, C. Wolverton, V. P. Dravid, Q. Yan and M. G. Kanatzidis, *Adv. Funct. Mater.*, 2018, **28**, 1801617.

14 A. Banik, T. Ghosh, R. Arora, M. Dutta, J. Pandey, S. Acharya, A. Soni, U. V. Waghmare and K. Biswas, *Energy Environ. Sci.*, 2019, **12**, 589–595.

15 S. H. Yang, T. J. Zhu, T. Sun, J. He, S. N. Zhang and X. B. Zhao, *Nanotechnology*, 2008, **19**, 245707.

16 Z. Bu, X. Zhang, B. Shan, J. Tang, H. Liu, Z. Chen, S. Lin, W. Li and Y. Pei, *Sci. Adv.*, 2021, **7**, eabf2738.

17 X. Zhang, J. Li, X. Wang, Z. Chen, J. Mao, Y. Chen and Y. Pei, *J. Am. Chem. Soc.*, 2018, **140**(46), 15883–15888.

18 S. Perumal, M. Samanta, T. Ghosh, U. S. Shenoy, A. K. Bohra, S. Bhattacharya, A. Singh, U. V. Waghmare and K. Biswas, *Joule*, 2019, **3**, 2565–2580.

19 D. Wu, L. D. Zhao, S. Hao, Q. Jiang, F. Zheng, J. W. Doak, H. Wu, H. Chi, Y. Gelbstein, C. Uher, C. Wolverton, M. Kanatzidis and J. He, *J. Am. Chem. Soc.*, 2014, **136**(32), 11412–11419.

20 K. S. Bayikadi, C. T. Wu, L. C. Chen, K. H. Chen, F. C. Chou and R. Sankar, *J. Mater. Chem. A*, 2020, **8**, 5332–5341.

21 Z. Zheng, X. Su, R. Deng, C. Stoumpos, H. Xie, W. Liu, Y. Yan, S. Hao, C. Uher, C. Wolverton, M. G. Kanatzidis and X. Tang, *J. Am. Chem. Soc.*, 2018, **140**(7), 2673–2686.

22 M. Hong, Z. G. Chen, L. Yang, Y. C. Zou, M. S. Dargusch, H. Wang and J. Zou, *Adv. Mater.*, 2018, **30**, 1705942.

23 J. Li, X. Zhang, X. Wang, Z. Bu, L. Zheng, B. Zhou, F. Xiong, Y. Chen and Y. Pei, *J. Am. Chem. Soc.*, 2018, **140**(47), 16190–16197.

24 L. Xie, Y. Chen, R. Liu, E. Song, T. Xing, T. Deng, Q. Song, J. Liu, R. Zheng, X. Gao, S. Bai and L. Chen, *Nano Energy*, 2020, **68**, 104347.

25 E. Nshimyimana, S. Hao, X. Su, C. Zhang, W. Liu, Y. Yan, C. Uher, C. Wolverton, M. G. Kanatzidis and X. Tang, *J. Mater. Chem. A*, 2020, **8**, 1193–1204.

26 M. Hong, K. Zheng, W. Lyv, M. Li, X. Qu, Q. Sun, S. Xu, J. Zou and Z. G. Chen, *Energy Environ. Sci.*, 2020, **13**, 1856–1864.

27 S. Perumal, P. Bellare, U. S. Shenoy, U. V. Waghmare and K. Biswas, *Chem. Mater.*, 2017, **29**, 10426–10435.

28 T. Xing, Q. Song, P. Qiu, Q. Zhang, X. Xia, J. Liao, R. Liu, H. Huang, J. Yang, S. Bai, D. Ren, X. Shi and L. Chen, *Natl. Sci. Rev.*, 2019, **6**, 944–954.

29 P. Acharyya, S. Roychowdhury, M. Samanta and K. Biswas, *J. Am. Chem. Soc.*, 2020, **142**(48), 20502–20508.

30 T. Xing, C. Zhu, Q. Song, H. Huang, J. Xiao, D. Ren, M. Shi, P. Qiu, X. Shi, F. Xu and L. Chen, *Adv. Mater.*, 2021, **33**, 2008773.

31 Y. F. Tsai, P. C. Wei, L. Chang, K. K. Wang, C. C. Yang, Y. C. Lai, C. R. Hsing, C. M. Wei, J. He, G. J. Snyder and H. J. Wu, *Adv. Mater.*, 2021, **33**, 1–8.

32 K. S. Bayikadi, R. Sankar, C. T. Wu, C. Xia, Y. Chen, L. C. Chen, K. H. Chen and F. C. Chou, *J. Mater. Chem. A*, 2019, **7**, 15181–15189.

33 J. W. Zhang, Z. W. Wu, B. Xiang, N. N. Zhou, J. L. Shi and J. X. Zhang, *ACS Appl. Mater. Interfaces*, 2020, **12**, 21863–21870.

34 B. Shan, S. Lin, Z. Bu, J. Tang, Z. Chen, X. Zhang, W. Li and Y. Pei, *J. Mater. Chem. A*, 2020, **8**, 3431–3437.

35 M. T. Agne, R. Hanus and G. J. Snyder, *Energy Environ. Sci.*, 2018, **11**, 609–616.

36 D. A. Baker, M. A. Paesler, G. Lucovsky, S. C. Agarwal and P. C. Taylor, *Phys. Rev. Lett.*, 2006, **96**, 255501.

37 U. Jayarathne, P. Chandrasekaran, A. F. Greene, J. T. Mague, S. Debeer, K. M. Lancaster, S. Sproules and J. P. Donahue, *Inorg. Chem.*, 2014, **53**(16), 8230–8241.

38 J. Cao, X. Y. Tan, N. Jia, D. Lan, S. F. D. Solco, K. Chen, S. W. Chien, H. Liu, C. K. I. Tan, Q. Zhu, J. Xu, Q. Yan and A. Suwardi, *Nanoscale*, 2022, **14**, 410–418.

39 H. S. Lee, B. S. Kim, C. W. Cho, M. W. Oh, B. K. Min, S. D. Park and H. W. Lee, *Acta Mater.*, 2015, **91**, 83–90.

40 R. Hanus, M. T. Agne, A. J. E. Rettie, Z. Chen, G. Tan, D. Y. Chung, M. G. Kanatzidis, Y. Pei, P. W. Voorhees and G. J. Snyder, *Adv. Mater.*, 2019, **31**, 1–10.

41 B. Jiang, W. Wang, S. Liu, Y. Wang, C. Wang, Y. Chen, L. Xie, M. Huang and J. He, *Science*, 2022, **377**, 208–213.

42 W. Li, S. Lin, B. Ge, J. Yang, W. Zhang and Y. Pei, *Advanced Science*, 2016, **3**, 1600196.
43 G. Tan, S. Hao, R. C. Hanus, X. Zhang, S. Anand, T. P. Bailey, A. J. E. Rettie, X. Su, C. Uher, V. P. Dravid, G. J. Snyder, C. Wolverton and M. G. Kanatzidis, *ACS Energy Lett.*, 2018, **3**, 705–712.
44 G. Xie, Z. Li, T. Luo, H. Bai, J. Sun, Y. Xiao, L. D. Zhao, J. Wu, G. Tan and X. Tang, *Nano Energy*, 2020, **69**, 104395.
45 G. J. Snyder and A. H. Snyder, Figure of Merit ZT of a Thermoelectric Device Defined from Materials Properties, *Energy Environ. Sci.*, 2017, **10**, 2280.
46 G. J. Snyder, Thermoelectric Power Generation: Efficiency and Compatibility, in *Thermoelectrics Handbook: Macro to Nano*, ed. D. M. Rowe, CRC Press, 2006, ch. 9.
47 G. Kresse and J. Furthmüller, *Comput. Mater. Sci.*, 1996, **6**, 15–50.
48 G. Kresse and J. Furthmüller, *Phys. Rev. B: Condens. Matter Mater. Phys.*, 1996, **54**(16), 11169–11186.
49 D. Joubert, *Phys. Rev. B: Condens. Matter Mater. Phys.*, 1999, **59**, 1758.
50 P. E. Blöchl, *Phys. Rev. B: Condens. Matter Mater. Phys.*, 1994, **50**, 17953.
51 J. P. Perdew and Y. Wang, *Phys. Rev. B: Condens. Matter Mater. Phys.*, 1992, **45**, 13244.
52 K. Momma and F. Izumi, *J. Appl. Crystallogr.*, 2011, **44**, 1272–1276.
53 P. E. Blöchl, O. Jepsen and O. K. Andersen, *Phys. Rev. B: Condens. Matter Mater. Phys.*, 1994, **49**, 16223.